Computers and Concrete, Vol. 1, No. 2 (2004) 169-188
DOI: http://dx.doi.org/10.12989/cac.2004.1.2.169

A coupled damage-viscoplasticity model for the analysis of localisation and size effects

J. F. Georgin†

URGC Structures, INSA de Lyon, Villeurbanne France,

L. J. Sluys‡

TU Delft, Faculty of Civil Engineering and Geosciences, Delft, The Netherlands

J. M. Reynouard‡†

URGC Structures, INSA de Lyon, Villeurbanne, France
(Received December 15, 2003, Accepted April 10, 2004)

Abstract. A coupled damage-viscoplasticity model is presented for the analysis of localisation and size effects. On one hand, viscosity helps to avoid mesh sensitivity because of the introduction of a length scale in the model and, on the other hand, enables to represent size effects. Size effects were analysed by means of three-point bending tests. Correlation between the fracture energy parameter measured experimentally and the density fracture energy modelling parameter is discussed. It has been shown that the dependence of nominal strength and fracture energy on size is determined by the ligament length in comparison with the width of the fracture process zone.

Keywords: damage viscoplasticity; fracture energy; size effect; localisation.

1. Introduction

An adequate prediction of cracking behaviour capturing both size and rate effects is the main difficulty in the modeling of concrete. Many finite element programs have adopted the smeared crack concept for dealing with tension behaviour where relative displacements of crack surfaces are represented by crack strains and the constitutive behaviour of cracked concrete is described in terms of stress-strain relationships in a continuum framework. Recent research (Möes, *et al.* 1999, Wells and Sluys 2001) deals with a new generation of modeling techniques based on incorporating discontinuities in the kinematic fields exploiting the partition of unity concept. This approach leads to an activation of discontinuities at arbitrary locations avoiding costly remeshing. The spatial orientation of the discontinuity surface is only determined by the mechanical state in the body. A combined continuum-discontinuous framework (Wells 2001, Simone, *et al.* 2003) for crack propagation

† Assistant Professor
‡ Associate Professor
‡† Professor

and strain localization allows to describe the fracture process in cementitious materials where a fracture process zone develops from smeared micro-cracks into a macro-crack (Otsuka and Date 2000).

The fracture process in softening materials cannot be described with a continuum rate-independent model. Recently, a new coupled damage-viscoplasticity model has been developed with excellent characteristics for the modelling of localisation under static and dynamic loading conditions (Georgin, *et al.* 2002). Viscoplasticity is known to be a suitable concept for the computational modelling of failure. The introduction of viscous terms in the constitutive model introduces a length scale effect and solves mesh dependence in localisation problems (Needleman 1988, Sluys 1992). The length scale effect in the Duvaut-Lions viscoplasticity model is constant (Georgin, *et al.* 2002). For this reason, the width of the localisation band is constant and does not narrow and finally will not collapse into a macro-crack of zero width when the strain reaches the ultimate strain. Furthermore, since the strain rate at ultimate strain is unequal to zero we have a viscous stress component. This viscous contribution of the stress causes that we cannot obtain a stress-free crack at ultimate strain. If the strain rate is increasing, which normally takes place at crack opening, even some rehardening effects can be observed in the crack. Both the narrowing localisation zone and the stress-free crack are features which can be modelled with the coupled damage-viscoplasticity model treated in this contribution.

Fracture energy is a significant parameter in localisation analyses representing the energy required for fracture. A RILEM recommendation (Hillerborg, *et al.* 1976, Petersson 1980a, b, Hillerborg 1985a, b, c) specifies an experimental method for the determination of the fracture energy (G_f) of mortar and concrete by means of stable three-point bending tests on notched beams. The last two decades, many investigations have been carried out to size effects (Bazant and Pfeiffer 1987, Bazant and Gettu 1992, Bazant 1996, Bazant and Planas 1998, Bazant 2000). More recently, size effect experiments of concrete revealed a fracture energy increase with increasing specimen size and un-notched ligament length (Wittmann, *et al.* 1990, Hu and Wittmann 2000, Duan, *et al.* 2002, Hu 2002, Duan, *et al.* 2003). In this paper, the RILEM test is simulated with the damage-viscoplasticity model in order to validate its ability to describe the fracture process properly. The model takes into account the amount of energy necessary to create a unit crack area in a proper way; the area under the load mid-span displacement curve divided by the area of the crack restores a consistent value of the dissipated energy.

2. Concrete model

The damage variable, associated with concrete failure processes, can be interpreted as the surface density of material defects (Kachanov 1986, Ju 1989), and will be defined as the ratio between the area occupied by created micro-cracks and the overall material area S. This definition states that the damage variable is a non decreasing parameter, since the reduction of the effective resisting section area $\tilde{S}$ will continuously increase until failure occurs.

$$\tilde{S} = (1 - D)S \tag{1}$$

in which D is the damage variable taking values between 0 (undamaged material) and 1 (completely damaged material). The stress-strain relationship in a coupled damage-viscoplastic medium is written as :

$$\sigma = (1-D)\mathbf{E}_0 : \boldsymbol{\varepsilon}^e = \mathbf{E} : (\boldsymbol{\varepsilon} - \boldsymbol{\varepsilon}^{vp}) \tag{2}$$

$$\sigma = (1-D)\tilde{\boldsymbol{\sigma}}$$

where σ is the nominal stress tensor (damage viscoplastic stress tensor) and $\tilde{\sigma}$ is the effective stress tensor (viscoplastic stress tensor), ε^e and ε^{vp} are the elastic and viscoplastic strain, respectively. We assume an isotropic scalar damage model. The degree of brittleness of the mechanical effect of progressive micro-cracking due to external loads is described by the single internal scalar variable D which degrades the initial stiffness tensor $\mathbf{E_0}$ such that the stiffness tensor $\mathbf{E}$ reads:

$$\mathbf{E} = (1-D)\mathbf{E}_0 \tag{3}$$

Viscoplasticity is formulated by means of a Duvaut-Lions approach (Duvaut and Lions 1972, Sluys 1992) according to

$$\dot{\boldsymbol{\varepsilon}}^{vp} = \frac{1}{\eta}\mathbf{E}^{-1} : (\sigma - \bar{\sigma}) \tag{4}$$

In which η is the viscosity parameter and $\bar{\sigma}$ is the damage-plastic stress tensor which results from:

$$\bar{\sigma} = (1-\bar{D})\mathbf{E}_0 : \boldsymbol{\varepsilon}^e = \mathbf{E} : (\boldsymbol{\varepsilon} - \boldsymbol{\varepsilon}^p) \tag{5}$$

$$\sigma = (1-\bar{D})\,\bar{\tilde{\sigma}}$$

Where ε^p is the rate-independent plastic strain and $\bar{D}$ is the rate-independent damage variable corresponding to the damage-plastic back-bone of the model.

The hardening/softening parameter κ, associated to the effective viscoplastic stress state $\tilde{\sigma}$, is updated by means of the following equation:

$$\dot{\kappa} = \frac{1}{\eta}(\kappa - \bar{\kappa}) \tag{6}$$

in which $\bar{\kappa}$ is the hardening/softening parameter corresponding to the effective plastic stress state $\bar{\tilde{\sigma}}$.

The plastic response is characterized in the effective plastic stress space and the yield surface is given by

$$F(\bar{\tilde{\sigma}}, \bar{\kappa}) \leq 0 \tag{7}$$

A non-smooth multisurface criterion (Fig. 1) is used to describe the material behaviour of concrete in tension and compression (Feenstra 1993). The employed yield surfaces F_i are function of invariants of the effective plastic stress tensor $\bar{\tilde{\sigma}}$ and the hardening parameter $\bar{\kappa}$. For tension, a Rankine yield function is used

$$F_t(\bar{\tilde{\sigma}}, \bar{\kappa}_t) = \bar{\tilde{\sigma}}_I - \bar{\tilde{\tau}}_t(\bar{\kappa}_t) \tag{8}$$

and for compression a Drucker-Prager yield function is used

$$F_c(\tilde{\tilde{\sigma}},\ \overline{\kappa_c}) = J_2(\tilde{\tilde{\mathbf{s}}}) + \beta_1 I_1(\tilde{\tilde{\sigma}}) - \beta_2 \tilde{\tilde{\tau}}_c(\overline{\kappa_c}) \tag{9}$$

where $\tilde{\tilde{\sigma}}_I$ is the major principal stress, $I_1(\tilde{\tilde{\sigma}})$ is the first invariant of the stress tensor, $J_2(\tilde{\tilde{\mathbf{s}}})$is the second invariant of the deviatoric stress tensor $\tilde{\tilde{\mathbf{s}}}$, β_1, and β_2 are two multiplying factors. $\tilde{\tilde{\tau}}_t$ and $\tilde{\tilde{\tau}}_c$ are respectively the equivalent stresses in tension and in compression. The effective cohesion capacities of the material given by $\tilde{\tilde{\tau}}_t$ and $\tilde{\tilde{\tau}}_c$ are linked to the cohesion capacities $\tilde{\tilde{\tau}}_t$ and $\tilde{\tilde{\tau}}_c$ as:

$$\overline{\tau}_t = (1 - \overline{D_t})\ \tilde{\tilde{\tau}}_t \tag{10a}$$

$$\overline{\tau}_c = (1 - \overline{D_c})\ \tilde{\tilde{\tau}}_c \tag{10b}$$

which is expressed by an analytically convenient function that is valid for tension and compression. It is consistent with the fact that experimentally observed stress-strain curves tend to attain zero-stress level asymptotically and is chosen according to

$$\overline{\tau}_x = f_{x0}[(1 + a_x)\exp(-b_x\overline{\kappa_x}) - a_x\exp(-2b_x\overline{\kappa_x})] \tag{11}$$

in which a_x and b_x are material parameters and f_{x0} is the initial tensile strength ($x = t$) or the compressive yield stress ($x = c$). The parameter a_c in Eq. (11) is defined from the following expression which is set by the ratio of compressive strength f_c over compressive yield stress f_{c0}:

$$a_c = \left[2\left(\frac{f_c}{f_{c0}}\right) - 1\right] + 2\sqrt{\left(\frac{f_c}{f_{c0}}\right)^2 - \left(\frac{f_c}{f_{c0}}\right)} \tag{12}$$

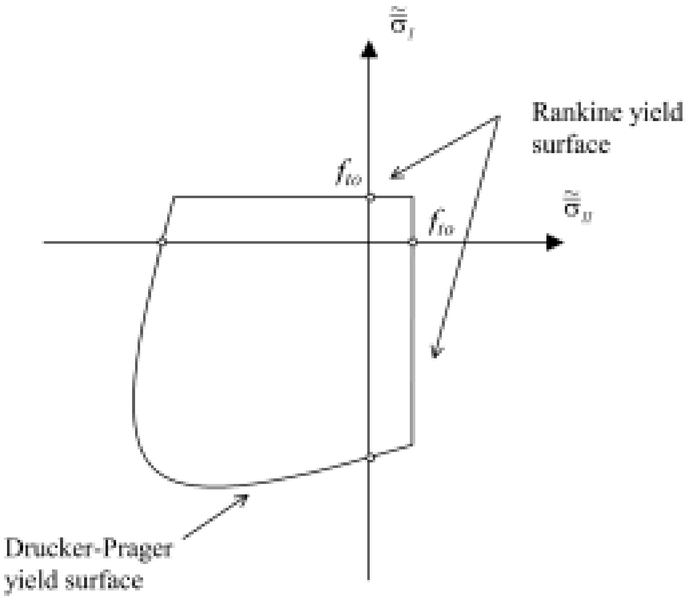

Fig. 1 Non-smooth yield criterion representation in the effective principal plastic stress space

For a ratio $\frac{f_c}{f_{c0}} = 0.3$, we have $a_c = 11.24$.

At the multisurface, corners in the stress space, the ambiguity of the plastic flow direction is removed using Koiter's rule (Koiter 1953, Maier 1969) by considering the contribution of each individual loading surface separately:

$$\dot{\boldsymbol{\varepsilon}}^p = \sum_{i=1}^{i=2} \dot{\lambda}_i \frac{\partial F_i}{\partial \tilde{\bar{\sigma}}} \tag{13}$$

where $\dot{\lambda}_i$ is the plastic multiplier associated to the plastic potential function F_i in tension or in compression.

The damage evolution laws have an exponential form according to:

$$1 - D_x = \exp(-c_x \kappa_x) \tag{14a}$$

$$1 - \bar{D}_x = \exp(-c_x \bar{\kappa}_x) \tag{14b}$$

respectively, dependent on the cumulated viscoplastic and plastic strain (see Eq. (6)), where c_x is a material parameter (Lee 1998, Meftah, *et al.* 2000, Nechnech 2000). In order to describe different behaviour under tensile (where subscript $x = t$) and compressive loading (where subscript $x = c$) as observed in test data, the mechanical damage variable is subdivided into two parts, one for tensile loading and one for compressive loading (Fig. 2) according to:

$$D(\kappa_t, \kappa_c) = 1 - (1 - D_t(\kappa_t))(1 - D_c(\kappa_c)) \tag{15}$$

The rate form of Eq. (2) leads to

$$\dot{\sigma} = (1 - D)\mathbf{E}_0 : (\dot{\boldsymbol{\varepsilon}} - \dot{\boldsymbol{\varepsilon}}^{vp}) - \dot{D}\, \mathbf{E}_0 : (\boldsymbol{\varepsilon} - \boldsymbol{\varepsilon}^{vp}) \tag{16}$$

Substituting Eq. (4) into Eq. (16) yields the following differential equation :

$$\dot{\sigma} + \left(\frac{1}{\eta} + \frac{\dot{D}}{1 - D}\right)\sigma = (1 - D)\mathbf{E}_0 : \dot{\boldsymbol{\varepsilon}} + \frac{1}{\eta}\bar{\sigma} \tag{17}$$

The stress update for the damage-viscoplasticity model is obtained by an Euler approach where the stress rate is determined with an approximate value from Eq. (17):

$$\sigma^{t+\Delta t} = C\left(\sigma^{t} + (1 - D^{t+\Delta t})\mathbf{E}_0 : \Delta\boldsymbol{\varepsilon} + \frac{\Delta \mathbf{t}}{\eta}\bar{\sigma}^{t+\Delta t}\right) \tag{18}$$

With $C = \dfrac{1}{1 + \dfrac{\Delta t}{\eta} + \dfrac{\Delta D}{1 - D^{t+\Delta t}}}$

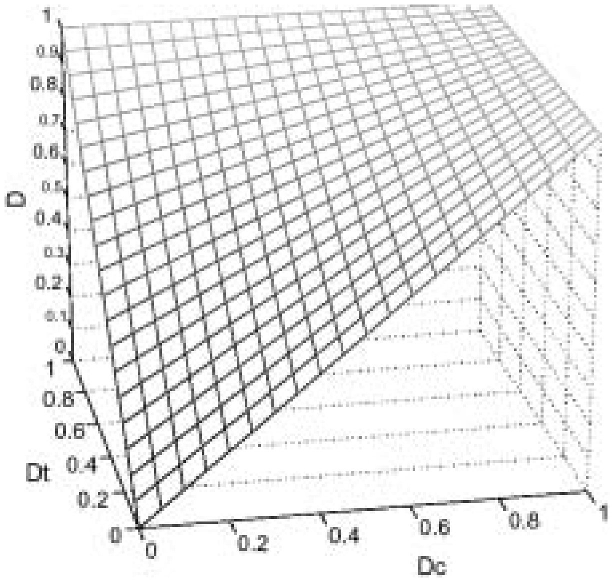

Fig. 2 Damage coupling representation

3. Regularisation aspects

The introduction of rate dependence in the coupled damage-plasticity model prevents the model from becoming ill-posed when strain softening takes place. It introduces a length scale parameter in the problem which is dependent on η. Both the narrowing localisation zone and the stress-free crack are features that are modelled with the coupled damage-viscoplasticity model.

If we differentiate Eq. (16) for a one-dimensional coupled damage-viscoplasticity element with respect to x and use the kinematic expression:

$$\varepsilon = \frac{\partial u}{\partial x} \tag{19}$$

and the one-dimensional equation of motion:

$$\frac{\partial \sigma}{\partial x} = \rho \frac{\partial^2 u}{\partial t^2} \tag{20}$$

with ρ the density, we obtain:

$$\eta\left(\rho \frac{\partial^3 u}{\partial t^3} - (1-D)\mathbf{E}_0 \frac{\partial^3 u}{\partial x^2 \partial t}\right) = \frac{\partial \bar{\sigma}}{\partial x} + \rho\left(1 + \frac{\eta \dot{D}}{1-D}\right) + \frac{\partial^2 u}{\partial t^2} \tag{21}$$

which is the wave equation for a one-dimensional coupled damage-viscoplastic element. We can distinguish three cases

(i) Rate independence
For this case $\eta = 0$ and the left-hand-side in Eq. (21) cancels. The problem is ill-posed in case of

statics and dynamics.

(ii) Rate dependence-statics

The inertia terms one and four cancel from Eq. (21) in the static case. The behaviour is set by the remaining third-order term. The problem is well-posed but approaches the ill-posed limit when the viscosity becomes zero ($\eta \to 0$) or the material is fully damaged ($D \to 1$).

(iii) Rate dependence-dynamics

All terms appear in Eq. (21), but the behaviour is governed by the two third-order terms. The problem remains well-posed if η>0.

From the second case it can be concluded that for the static case the regularising effect, which is constant for the viscoplastic model, decreases upon increasing damage and vanishes when $D = 1$. This results in a narrowing localisation zone and a stress drop to zero at full crack opening. To demonstrate this, we present the numerical result of a bar (Fig. 3) subjected to an imposed displacement for different meshes (20, 50 and 100 elements). The material parameters are $E_o = 35000$ MPa, $f_{to} = 4$ MPa, $a_t = -0.5$, $b_t = 600$ and $c_t = 358.7$. The damage viscoplasticity model gives the same force displacement curve for the three meshes (see Fig. 4). Furthermore, we can observe that the stress drops to zero after failure. A slight difference of the finite element solution appears when the stress is almost zero. In this case the length scale (=regularising) effect approaches zero and the corresponding width of the localisation zone becomes smaller than the finite element size. The small mesh dependence in the tail of the curve is not related to the classical

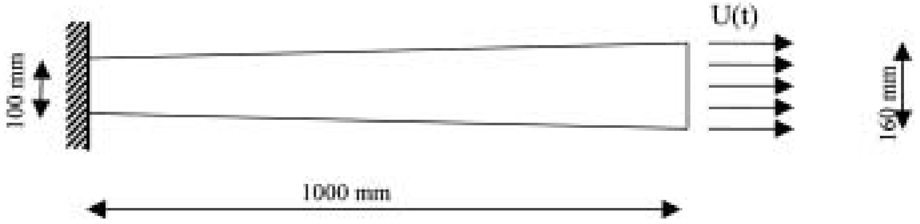

Fig. 3 Geometry of the uniaxial bar

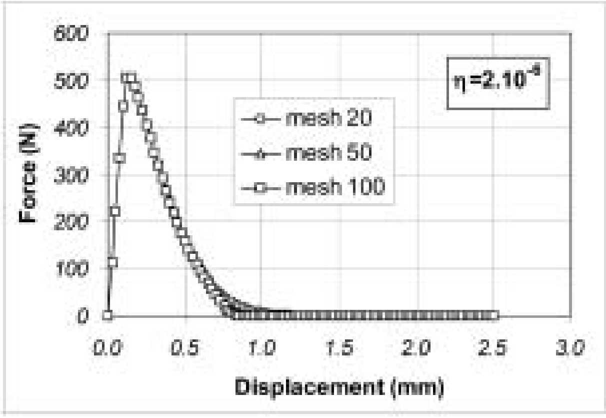

Fig. 4 Uniaxial force-displacement response

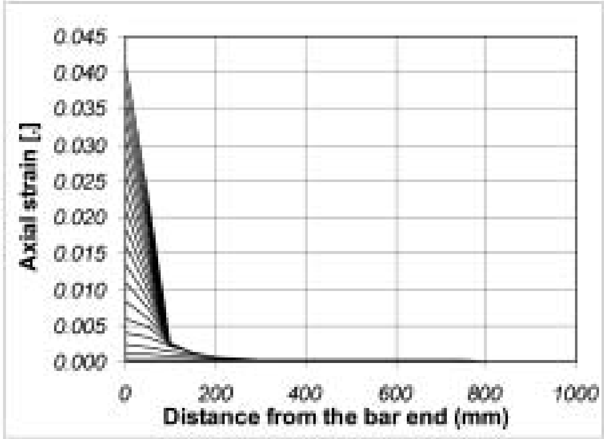

Fig. 5 Axial strain gradient (mesh 20)

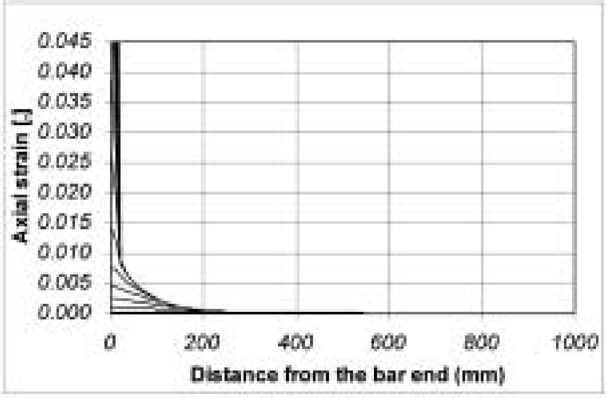

Fig. 6 Axial strain gradients (mesh 100)

mesh dependence problem in strain-softening media. From the stroboscopic evolution of the axial strain in Figs. 5 and 6 we can see that the crack band narrows when the strain increases. The band width even becomes smaller than the finite element size, which causes that the strain is more localised for the analysis with 100 elements (Fig. 6) than for the analysis with 20 elements (Fig. 5). With the 100 elements mesh, the narrowing band width can be captured in a better way.

The predictive capacity of the model is illustrated by means of the Nooru-Mohamed test which is a notched specimen subjected to a mixed mode loading. Fig. 7 shows the configuration of the mixed-mode plane concrete fracture test, analyzed experimentally by Nooru-Mohamed, *et al.* (1993). The Double-Edge-Notched (DEN) specimen was placed in a special loading frame to allow for the analysis of various loading paths both in normal and shear direction. In this work, the numerical simulation was carried out in case of load-path 2 where the axial tensile and the lateral shear load were applied such that the associated displacement ratio is constant and equal to 1.0. The material parameters are $E_o = 32800$ MPa, $\nu = 0.2$, $f_{to} = 3.8$ MPa, $a_t = -0.5$, $b_t = 570$, $c_t = 422$, $f_c = 46$ MPa, $a_c = 11.2444$, $b_c = 304.62$, $c_c = 66$ and $\eta = 2.10^{-6}$. We can observe in Fig. 8 the crack pattern from the computational analysis and the experimental test. The propagation path of the band of

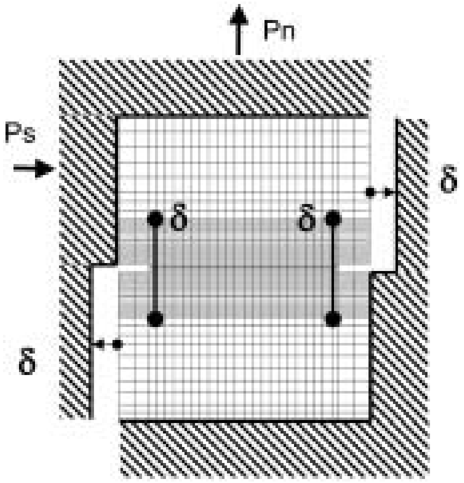

Fig. 7 Layout of the Nooru Mohamed test and mesh configuration

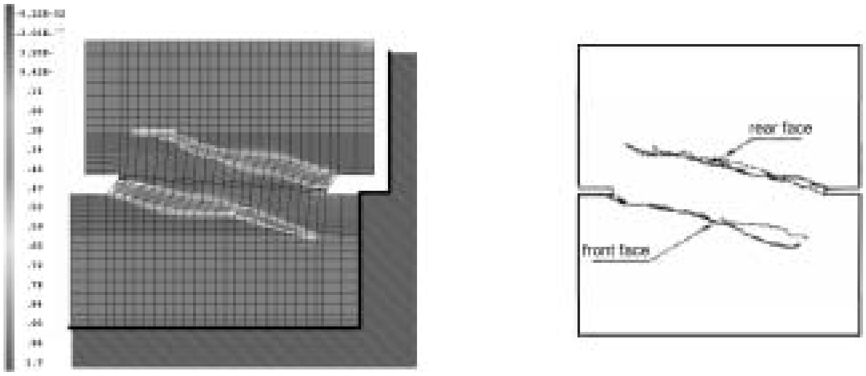

Map of the damage variable Dt   Experimental crack pattern (Nooru-Mohamed, et al. 1993)

Fig. 8 Comparison of the numerical and experimental crack pattern

localization into the specimen is clearly independent of the mesh in contrast with numerical results obtained with a rate-independent model and the crack situation is in good agreement with the experimental one. Fig. 9 shows the experimentally determined and numerically simulated relations between the tensile load P_n and the average normal displacement δ_n, between the shear force P_s and the average shear displacement δ_s.

The mode I cracking model shows good agreement with the experimental response for the mixed mode loading case. Nevertheless, we observe in Fig. 9 differences in the shear and the normal response curves. This study showed that the boundary conditions are very crucial. Imposed displacements are in agreement with the fact that in the experiment only top and bottom of the specimen are glued to the apparatus. We clearly observe that the model is too brittle in comparison to the experiment specifically in the descending branch of the normal behaviour. This brittleness is due to the shape of the softening curve adopted (Eq. (11)).

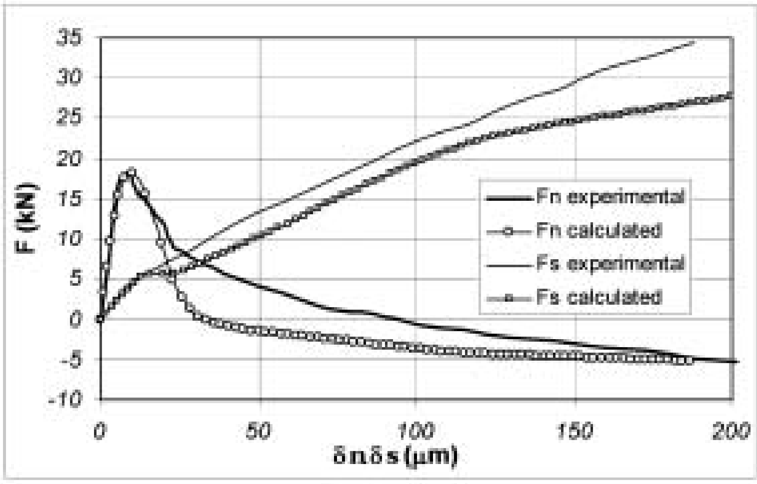

Fig. 9 Force displacement response in normal and shear direction

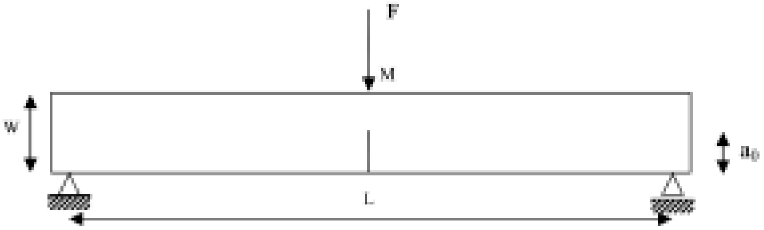

Fig. 10 Three-point bending test

Table 1 Geometrical characteristics

Type	L [mm]	W [mm]	a_0 [mm]
A	80	10	5
B	400	50	25
C	800	100	50
D	1600	200	100
E	2400	300	150

4. Fracture energy - Size effect

The ability of the damage-viscoplasticity model to describe size effects in fracture is illustrated by comparing the numerical results of the three point bending test for five different specimen sizes (see Fig. 10 and Table 1). The fracture energy parameter G_f commonly called the specific fracture energy, represents the consumed energy in order to create a unit crack area on average over the ligament length (W-a_o). Experimentally, it can be estimated by using the work of fracture method (Hillerborg 1985) from the force versus displacement curve in which the force is applied at location M (see Fig. 10). We can obtain a numerical estimation of G_f from the curves shown in Fig. 11 and

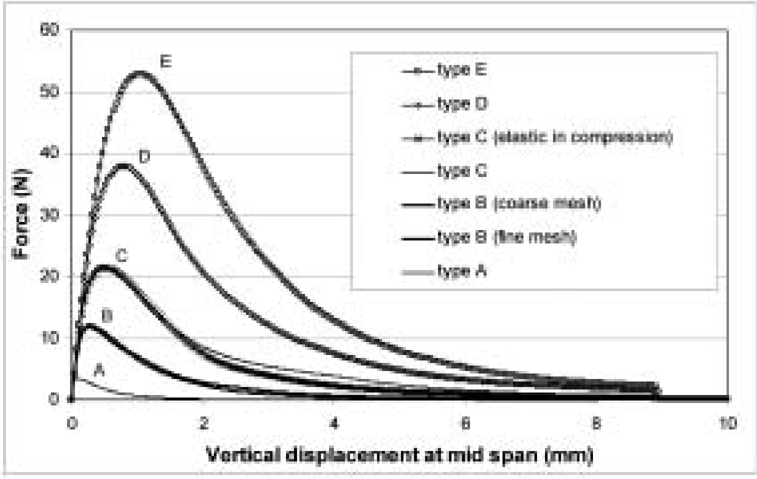

Fig. 11 Force versus vertical displacement at mid span

with the help of the following expression:

$$G_f = \frac{Area\ under\ force\ displacement\ curve}{Crack\ area} \tag{22}$$

The material parameters used in these calculations are the Young's modulus $E = 30$ GPa, compressive strength $f_c = 42$ MPa, tensile strength $f_{to} = 4.2$ MPa, the viscosity parameter $\eta = 2.10^{-6}$s, $a_t = -0.5$, $b_t = 45.$ and $c_t = 26.9$. We can define a model parameter denoted as density fracture energy R which is the area under the equivalent stress-hardening parameter curve (Eq. (11)). Then, we have the following relationship which leads to $R = 0.07$ N/mm^2 with the above parameters:

$$R = \left(1 + \frac{a_t}{2}\right)\frac{f_{to}}{b_t} \tag{23}$$

The link between the density fracture energy R with the parameter G_f does not appear clearly. Often, we state R as the ratio of the specific fracture energy by the characteristic length which is supposed to be the constant width of the localisation band in the failure zone. But as we observed previously, the width of the localization zone is not constant in experimental observations as well as in this modelling approach. Moreover, from this point of view, distribution of the fracture energy is supposed to be constant over the ligament which is maybe not true. For this reason, we define the local fracture energy g_f (Duan, *et al.* 2002) according to:

$$g_f = \int_{-\frac{\lambda}{2}}^{+\frac{\lambda}{2}}\left(\int_{t=0}^{t=\infty}\sigma_{ii}d\varepsilon_{ii}\right)dx \tag{24}$$

in which, x is the coordinate perpendicular to the crack path and λ is an integration length which should be larger than the width of the localisation band. In Eq. (24), term between brackets corresponds in a rate-independent material case to the density fracture energy R, previously defined in a modelling aspect. Moreover, the local fracture energy is coupled to the global fracture energy via

$$G_f = \frac{1}{W-a_0}\int_0^{W-a_0} g_f(y)dy \tag{25}$$

in which y is the vertical axis along the crack. The specific fracture energy G_f is in fact an average of different local fracture energy $g_f(y)$ values over the ligament (W–a_o).

Results of the finite element calculations are shown in Fig. 11 in terms of forces versus displacements. A mesh sensitivity study was carried out in order to check the uniqueness of the finite element solution. We can observe in Fig. 11 that the finite element solutions of two different

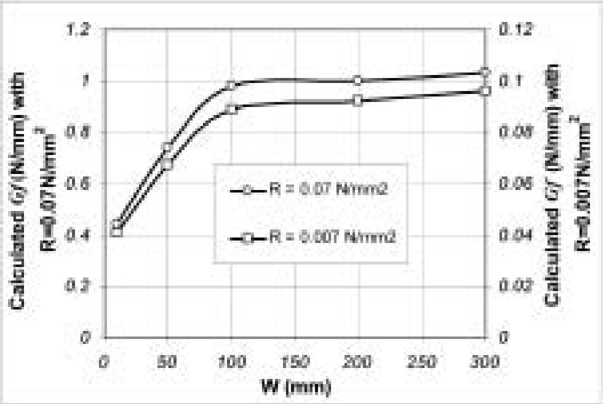

Fig. 12 Specific fracture energy G_f versus size for two density fracture energy R values

Table 2 Calculated fracture energy G_f

Beam Type	Area under F-u curve [Nmm]	Crack length [mm]	G_f [Nmm/mm]
A	2.22	5	0.44
B	18.49	25	0.74
C	49.31	50	0.98
C (elastic in compression)	43.95	50	0.88
D	99.75	100	0.99
E	155.73	150	1.03

Table 3 Different meshes

Type A, B (coarse mesh)	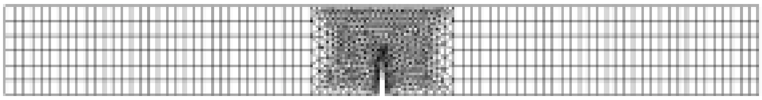
Type B (fine mesh), C, D	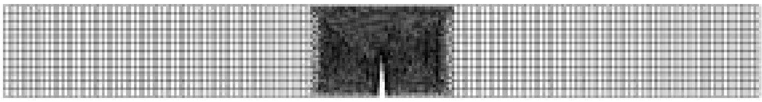
Type E	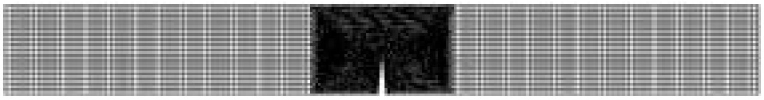

meshes in case of type B are similar. The meshes are presented in Table 3. Table 2 gives the numerical values obtained with Eq. (22). In Fig. 12, evolution of the calculated G_f versus the characteristic dimension of the beam W is plotted. We can clearly see that G_f depends on the size W for small sizes of the beam and G_F is the asymptotic value of G_f when the specimen is large. This observation was experimentally demonstrated by several authors (Wittmann, *et al.* 1990, Van Vliet and Van Mier 1998). Moreover, simulations of the three point bending test with a density fracture energy $R = 0.007$ N/mm^2 which is ten times smaller than in the previous analysis, demonstrates the consistency of this approach. These numerical data demonstrate that by taking a material viscosity into account, a proper description of the failure process of concrete is made possible. Viscosity parameter η and fracture energy density R characterize the cracking process in concrete. Inverse methods must be used to determine these model parameters R and η.

The size effect is understood as the dependence of the structural strength on the structural size. The nominal strength σ_{Nu} is conventionally defined as the value of the so-called nominal stress σ_N at the peak load $F_{\max}$ (Bazant and Planas 1998) calculated as:

$$\sigma_{Nu} = C_N \frac{\mathbf{F}_{\max}}{bW} \tag{26}$$

where b is the specimen thickness and C_N is a coefficient introduced for convenience. In a log-log plot, the nominal strength versus specimen size law obtained with the coupled damage-viscoplasticity model can be fitted as shown in Fig. 13 to the well-known size effect law proposed by Bazant and Planas (1998):

$$\sigma_N = \frac{Bf_t'}{\sqrt{1 + W/W_0}} \tag{27}$$

in which f_t' is the tensile strength which is introduced only for dimensional purposes, B is a dimensionless constant and W_0 is a constant with the dimension of length. The two last parameters depend on the fracture properties of the material and on the geometrical shape of the structure, but not on the structure size. This size effect law represents the variation of the nominal strength σ_{Nu} with size W. We observe in Fig. 13 that the numerical size effect is well predicted by the size effect law (Eq. (27)).

As pointed out in the introduction, many studies are concerned with the analysis of size effects and the analysis of fracture energy versus size and ligament length. The aim of this work is to show with the help of the previously presented model that the size dependence of the fracture energy can be explained by a non-uniform distribution of the local fracture energy g_f along the crack path.

When the material is rate-dependent, the density fracture energy which is actually consumed $R(\dot{\varepsilon})$, is higher than the density fracture energy R consumed in a rate-independent material. $R(\dot{\varepsilon})$ can be calculated with the help of the stress-strain curves according to:

$$R(\dot{\varepsilon}) = \int_{t=0}^{t=\infty} \sigma_{xx} d\varepsilon_{xx} + \int_{t=0}^{t=\infty} \sigma_{yy} d\varepsilon_{yy} + \int_{t=0}^{t=\infty} \sigma_{xy} d\gamma_{xy} \tag{28}$$

For convenience, we take $\mathbf{R}=R(\dot{\varepsilon})$ in the following. Distributions of the density energy $\mathbf{R}$ over the fracture process zone (FPZ) were numerically calculated in case of the type A, B C and D and are presented in Figs. 16, 17, 18 and 19, respectively. The data processing of results from type F

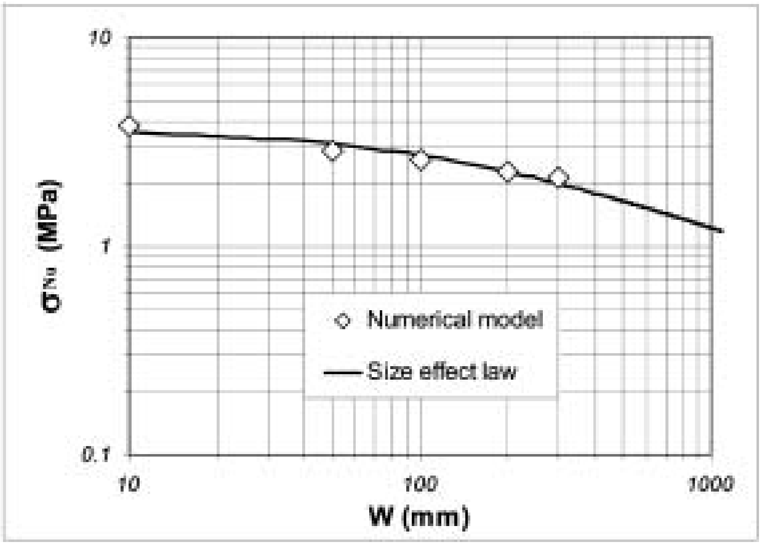

Fig. 13 Size effect from numerical analysis compared to the size effect law

was not possible for reasons of limiting computer memory size. One particular analysis in the third case C is the compressive behavior which is kept elastic in order to measure the contribution of the non-linear compressive behavior to the fracture energy G_f. The axes used for representation of the **R** distribution are clearly shown in Figs. 14 and 15. In order to compare the energy distribution along the crack path for different sizes of the beam, the *Y* axis was normalized to have *Y* equal to zero at the tip of the pre-cracked beam and *Y* equal to one at the top of the beam. In the *X* direction, the origin was taken at the tip of the pre-cracked beam and coordinate *x* was compared to the integration length λ_i (Figs. 14 and 15) of the corresponding type geometry $i \in \{A, B, C, D\}$ such that:

$$X = \frac{x}{\lambda_i} \text{ and } \frac{L_A}{\lambda_A} = \frac{L_B}{\lambda_B} = \frac{L_i}{\lambda_i} = Cte \tag{29}$$

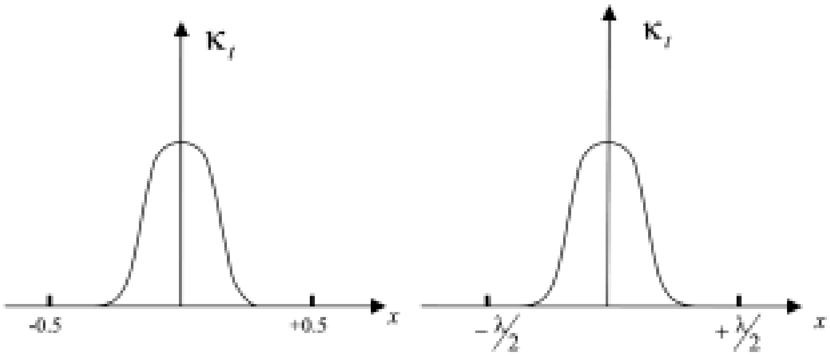

a) Normalized coordinate X b) Absolute coordinate x

Fig. 14 The hardening variable distribution in the transversal direction of the localization band

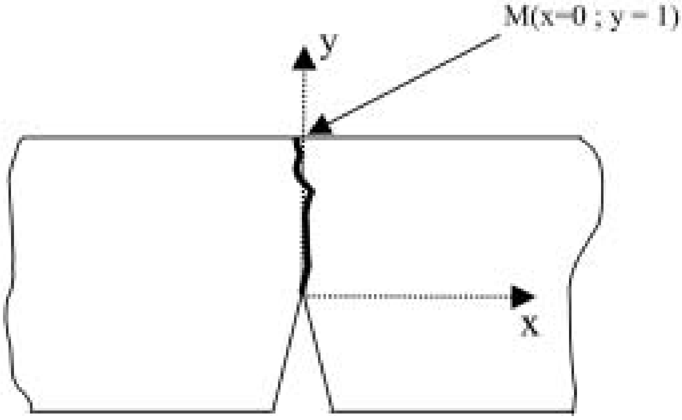

Fig. 15 Axes and coordinates on the FPZ

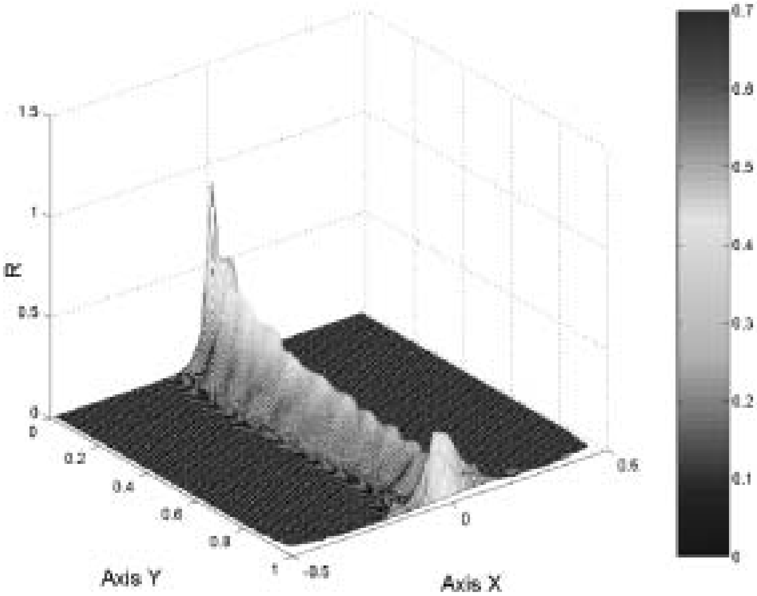

Fig. 16 Distribution of the density fracture energy over crack pattern (Type A)

The objective of this study is to find with the help of the computational model the origin of the dependence of the specific fracture energy G_f shown in Fig. 12 on size. We observe in all distributions (except in Type B with elastic behavior in compression) a high level of density energy at the point M ($X = 0$ and $Y = 1$). Differences between both cases with or without non-linear behavior in compression can not be neglected in terms of force versus displacement response (see Fig. 11) and in terms of the value of the specific fracture energy G_f (see Table 2). Nevertheless, the size effect observed both numerically and experimentally has not its roots in this point. Fig. 20 shows the evolution of the density energy along the crack pattern. The density fracture energy is decreasing while the size of the beam is increasing. Thus, distribution of energy density along the crack path can not explain the size effect. The explanation should come from the analysis of

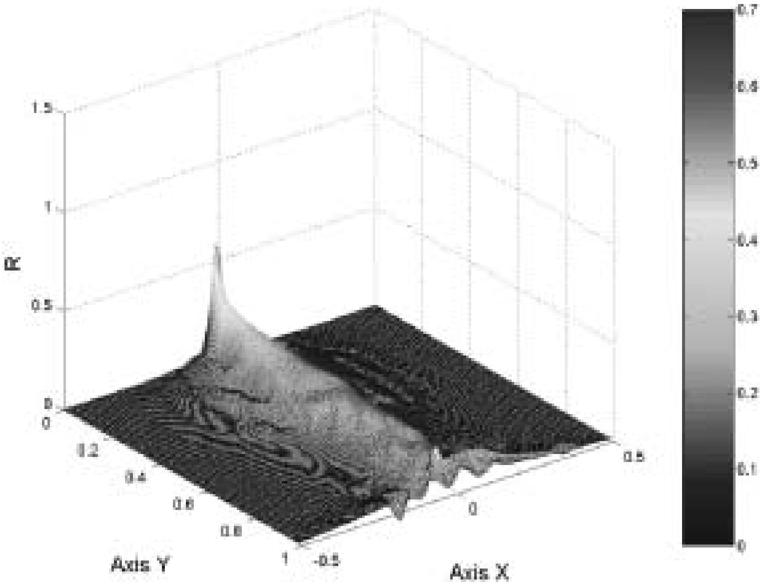

Fig. 17 Distribution of the density fracture energy over crack pattern (Type B)

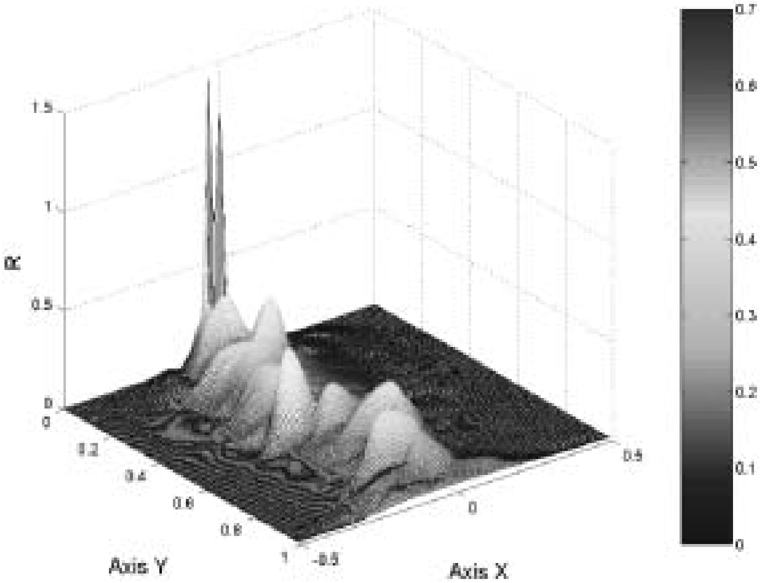

Fig. 18 Distribution of the density fracture energy over crack pattern (Type C elastic in compression)

distribution of the consumed energy in the direction transversal to the crack.

The local fracture energy g_f defined previously in Eq. (24) can be estimated with the following expression all along the FPZ:

$$g_{f_i} = \int_{-0.5}^{+0.5} R(\dot{\varepsilon})\lambda_i \; dX \qquad i \in \{A, B, C, D\} \qquad (30)$$

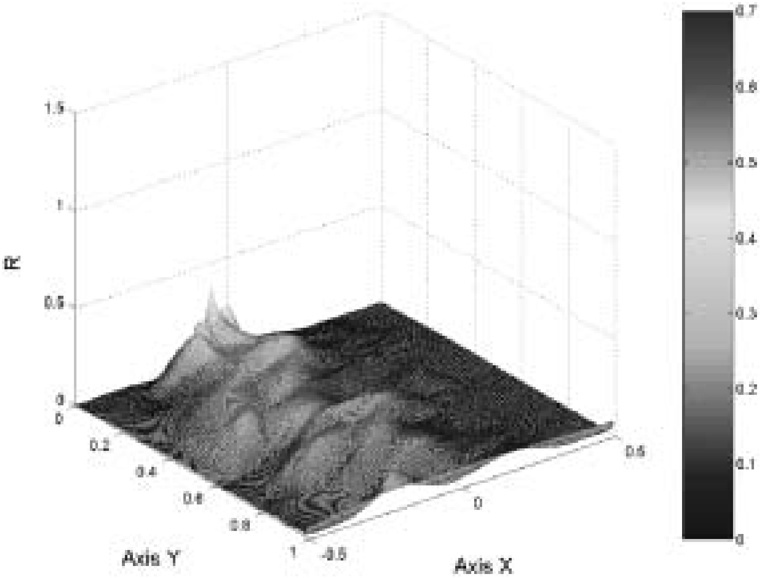

Fig. 19 Distribution of the density fracture energy over crack pattern (Type D)

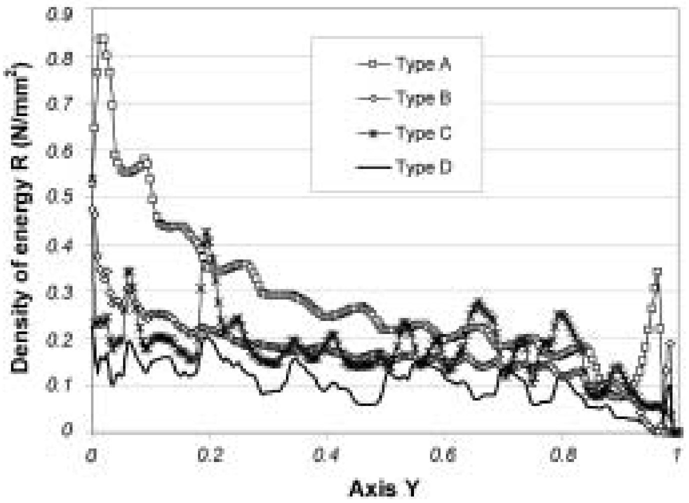

Fig. 20 Evolution of **R** along the crack pattern

Comparisons of the type A, B, C and D yield some interesting arguments with respect to the size effect analysis. The noisy data for the type C and D come from the number of finite elements which is not enough to describe the gradient of deformation inside the localization band which is similar irrespective of the type of beam. But, the number of elements used in type C and D was defined by the computer capacity. Consequently, an insufficient number of finite elements for larger beam sizes on top of the numerical interpolation procedure to determine the map of the evolution energy consumption into the FPZ lead to a more bumpy solution for C and D. Nevertheless, g_f versus coordinates Y curves drawn in Fig. 21 show a clear trend. The evolutions of the local fracture energy g_f are similar for the cases of the type C and D which can explain the fact that for large

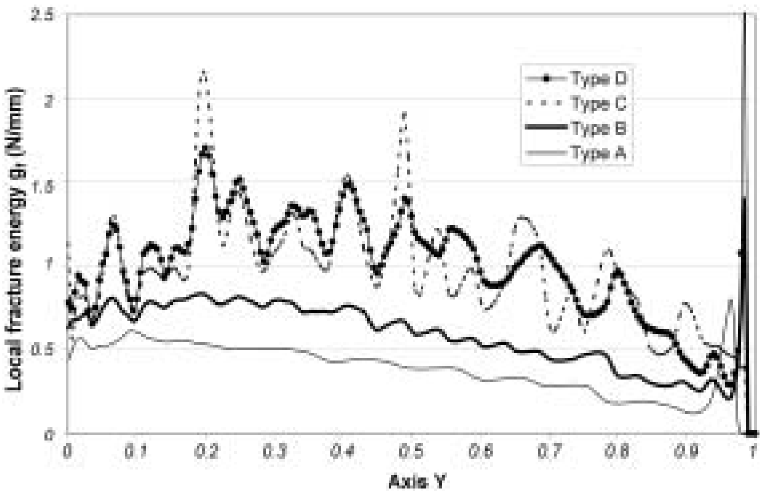

Fig. 21 Evolution of the local fracture energy G_f along the crack path

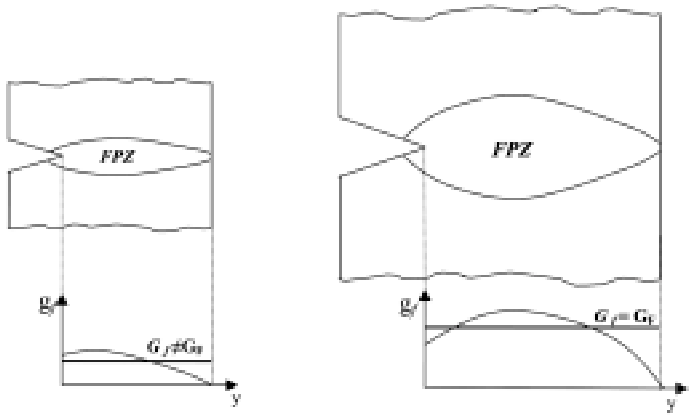

Fig. 22 Distribution of the local fracture energy along the FPZ

sizes the global fracture energy is size independent. The specific fracture energy G_f is evaluated from the area under the non-uniform curves of the local fracture energy curves via:

$$G_f = \int_0^1 g_f(Y) \; dY \tag{31}$$

In smaller specimens, the width of the FPZ is smaller than the internal characteristic length of the material which depends on its micro-structure (type of aggregate, sand and cement). In other words, this means that the FPZ may completely develop in large beams before failure of the beam occurs, as schematized in Fig 22. Experimental observations made by Otsuka and Date (2000) with the acoustic emission technique in terms of volume of energy consumed are in a good agreement with our conclusions. It seems to indicate that the length of the ligament influences the dependence of G_f more than the size W. This is the reason why dependency of G_f is experimentally observed on beams with the same size and different ligament length (Duan, *et al.* 2003).

5. Conclusions

This work shows that a coupled damage-viscoplasticity model is a suitable concept for the computational modeling of failure. Both the narrowing localisation zone and the stress-free crack are features which can be modelled with this approach. The numerical results for the three point bending tests show for a given material set (R,η), that the dissipated energy in the localization zone of the beam, firstly, depends on the size, and secondly, tends to a constant value with increasing size which is consistent with experiments. The dependence of the fracture energy is explained because the FPZ can not develop completely in the transversal direction to the crack or localization band for a smaller beam. Indeed, the width of the localization band commonly called the characteristic length is fixed by the concrete micro-structure. In this modeling approach, the characteristic length is defined by the viscosity parameter. In smaller specimens, the width of the localization band is lower than the characteristic length because the FPZ develops slower in transversal direction than the crack propagates in vertical direction which explains the size effect in smaller specimens. Consequently the dependence of parameters as nominal strength or fracture energy on size is more a matter of ligament length in relation to the material properties (characteristic length).

References

Bazant, Z. P. (1996), "Size effect aspects of measurement of fracture characteristics of quasibrittle material", *Advanced Cement Based Materials*, **4**, 128-137.

Bazant, Z. P. (2000), "Size effect", *Int. J. Solids Struct.*, **37**, 69-80.

Bazant, Z. P. and Gettu, R. (1992), "Rate effects and load relaxation in static fracture of concrete", *ACI Materials J.*, **89**(5), 456-468.

Bazant, Z. P. and Pfeiffer, P. A. (1987), "Determination of fracture energy from size effect and brittleness number", *ACI Materials*.

Bazant, Z. P. and Planas, J. (1998), "Fracture and size effect in concrete and other quasibrittle materials", *CRC Press*.

Duan, K., Hu, X., *et al.* (2002), "Boundary effect on concrete fracture and non-constant fracture energy distribution", *Eng. Fracture Mech.*, **70**, 2257-2268.

Duan, K., Hu, X., *et al.* (2002), "Explanation of size effect in concrete fracture using non-uniform energy distribution", *Materials Struct.*, **35**, 326-331.

Duan, K., Hu, X., *et al.* (2003), "Thickness effect on fracture energy of cementious materials", *Cement Concrete Comp.*, **33**, 499-507.

Duvaut, G. and Lions, J. L. (1972), *Les inequations en Mechanique et en Physique*. Paris.

Feenstra, P. H. (1993). "Computational aspects of biaxial stress in plain and reinforced concrete", Doctoral Thesis, Delft University of Technology**:** 149.

Georgin, J. F., Nechnech, W., *et al.* (2002), "A coupled damage-viscoplasticity model for localisation problem", *Proc. Fifth World Congress on Computational Mechanics*, Vol I, 428 Vienna, Austria.

Hillerborg, A. (1985a), "Determination of the fracture energy of mortar and concrete by means of three-point bend tests on notched beams" *50-FMC Committe Fracture Mechanics of Concrete*, **18**(106): 285-290.

Hillerborg, A. (1985b), "Results of three comparative test series for determining the fracture energy Gf of concrete", *Materials Struct.*, **18**(107), 407-413.

Hillerborg, A. (1985c), "The theoretical basis of a method to determine the fracture energy Gf of concrete", *Materials Struct.*, **18**(106), 291-296.

Hillerborg, A. and Modeer, M., *et al.* (1976), "Analysis of crack formation and crack growth in concrete by means of fracture mechanics and finite elements", *Cement Concrete Res.* **6**, 773-782.

Hu, X. and Wittmann, F. H. (2000), "Size effect on toughness induced by crack close to free surface", *Eng.*

Fracture Mech., **65**, 209-221.

Hu, X. Z. (2002), “An asymptotic approach to size effect on fracture toughness and fracture energy of composites”, *Eng. Fracture Mech.*, **69**, 555-564.

Ju, J. W. (1989), “On energy-based coupled elastoplastic damage theories: Constitutive modeling and computational aspects”, *Int. J. Solids Struct.*, **25**(7), 803-833.

Kachanov, L. M. (1986), *Introduction to Continuum Damage Mechanics*. Dordrecht, Martinus Nijhoff.

Koiter, W. T. (1953), “Stress-strain relations, uniqueness and variational theorems for elastic-plastic materials with a singular yield surface”, *Q. Appl. Math*, **3**.

Lee, J. (1998), “Theory and implementation of plastic-damage model for concrete structures under cyclic and dynamic loading”, Berkeley, University of California**:** 151.

Maier, G. (1969), “Linear flows-laws of elastoplasticity: a unified general approach”, *Lincei-Rend. Sci. Fis. Mat. Nat.*, **47**. 266-276.

Meftah, F. and Nechnech, W., *et al.* (2000), “An elasto-plastic damage model for plain concrete subjected to combined mechanical and high temperatures loads”, *14th Engineering Mechanical Conference (A.S.C.E)*, Austin U.S.A.

Möes, N. and Dolbow, J., *et al.* (1999), “A finite element method for crack growth without remeshing”, *Int. J. Num. Meth. Eng.*, **46**(1), 131-150.

Nechnech, W. (2000), Contribution à l'étude numérique du comportement du béton et des structures en béton armé soumises à des sollicitations thermiques et mécaniques couplées - Une approche thermo-élasto-plastique endommageable. LYON, INSA**:** 222.

Needleman, A. (1988), “Material rate dependence and mesh sensitivity on localisation problems”, *Comp. Meth. Appl. Mech. Eng.*, **67**, 69-86.

Nooru-Mohamed, M. and Schlangen, B. E., *et al.* (1993), “Experimental and numerical study on the behavior of concrete subjected to biaxial tension an shear”, *Advanced Cement Based Materials*, **1**, 22-37.

Otsuka, K. and Date, H. (2000), “Fracture process zone in concrete tension specimen”, *Eng. Fracture Mech.*, **65**, 111-131.

Petersson, P. E. (1980a), “Fracture energy of concrete: method of determination”, *Cement Concrete Comp.*, **10**, 78-89.

Petersson, P. E. (1980b), “Fracture energy of concrete: practical performance and experimental results”, *Cement Concrete Res.*, **10**, 91-101.

Simone, A. and Sluys, L. J., *et al.* (2003), “Combined continuous/discontinuous failure of cementitious composites”, EURO-C 2003,133-137, Swets & Zeitlinger, Lisse.

Sluys, L. J. (1992), “Wave propagation, localisation and dispersion in softening solids”, Doctoral Thesis, Delft University of Technology **173**.

Van Vliet, M. R. A. and Van Mier, J. G. M. (1998), “Experimental investigation of size effect in concrete under uniaxial tension”, FRAMCOS -III, Gifu, AEDIFICATIO.

Wells, G. N. (2001), “Discontinuous modelling of strain localisation and failure”, Doctoral Thesis, Faculty of Civil Engineering and Geosciences. Delft: 171.

Wells, G. N. and Sluys, L. J. (2001), “A new method for modelling cohesive cracks using finite elements”, *Int. J. Num. Meth. Eng.*, **50**, 2667-2682.

Wittmann, F. H. and Mirashi, H., *et al.* (1990), “Size effect on fracture energy of concrete”, *Eng. Fracture Mech.*, **35**(1/2/3), 107-115.

NB